doi:10.1038/nature05497

LETTERS

Dark matter maps reveal cosmic scaffolding

Richard Massey[1], Jason Rhodes[1,2], Richard Ellis[1], Nick Scoville[1], Alexie Leauthaud[3], Alexis Finoguenov[4], Peter Capak[1], David Bacon[5], Hervé Aussel[6], Jean-Paul Kneib[3], Anton Koekemoer[7], Henry McCracken[8], Bahram Mobasher[7], Sandrine Pires[9], Alexandre Refregier[6], Shunji Sasaki[10], Jean-Luc Starck[9], Yoshi Taniguchi[10], Andy Taylor[5] & James Taylor[11]

Ordinary baryonic particles (such as protons and neutrons) account for only one-sixth of the total matter in the Universe[1–3]. The remainder is a mysterious 'dark matter' component, which does not interact via electromagnetism and thus neither emits nor reflects light. As dark matter cannot be seen directly using traditional observations, very little is currently known about its properties. It does interact via gravity, and is most effectively probed through gravitational lensing: the deflection of light from distant galaxies by the gravitational attraction of foreground mass concentrations[4,5]. This is a purely geometrical effect that is free of astrophysical assumptions and sensitive to all matter—whether baryonic or dark[6,7]. Here we show high-fidelity maps of the large-scale distribution of dark matter, resolved in both angle and depth. We find a loose network of filaments, growing over time, which intersect in massive structures at the locations of clusters of galaxies. Our results are consistent with predictions of gravitationally induced structure formation[8,9], in which the initial, smooth distribution of dark matter collapses into filaments then into clusters, forming a gravitational scaffold into which gas can accumulate, and stars can be built[10].

The Hubble Space Telescope (HST) Cosmic Evolution Survey (COSMOS) is the largest contiguous expanse of high-resolution astronomical imaging obtained from space[11]. 575 slightly overlapping pointings of the Advanced Camera for Surveys (ACS) Wide Field Camera cover a region of 1.637 square degrees (more details about the COSMOS survey are available at www.astro.caltech.edu/~cosmos). We measure the shapes of half a million distant galaxies[12], and use their observed distortion (compare with Supplementary Fig. 1) to reconstruct the distribution of intervening mass, projected along our line of sight (Fig. 1). A realization of noise in our mass map, including most spurious instrumental or systematic effects, is provided by the '*B*-mode' signal. This is an additional degree of freedom in the data, which is not produced by gravitational lensing, and so is expected to be zero in the absence of systematics[13]. Assuming a gaussian noise distribution, the relative number of pixels above and below the first contour in the *B*-mode suggests that this

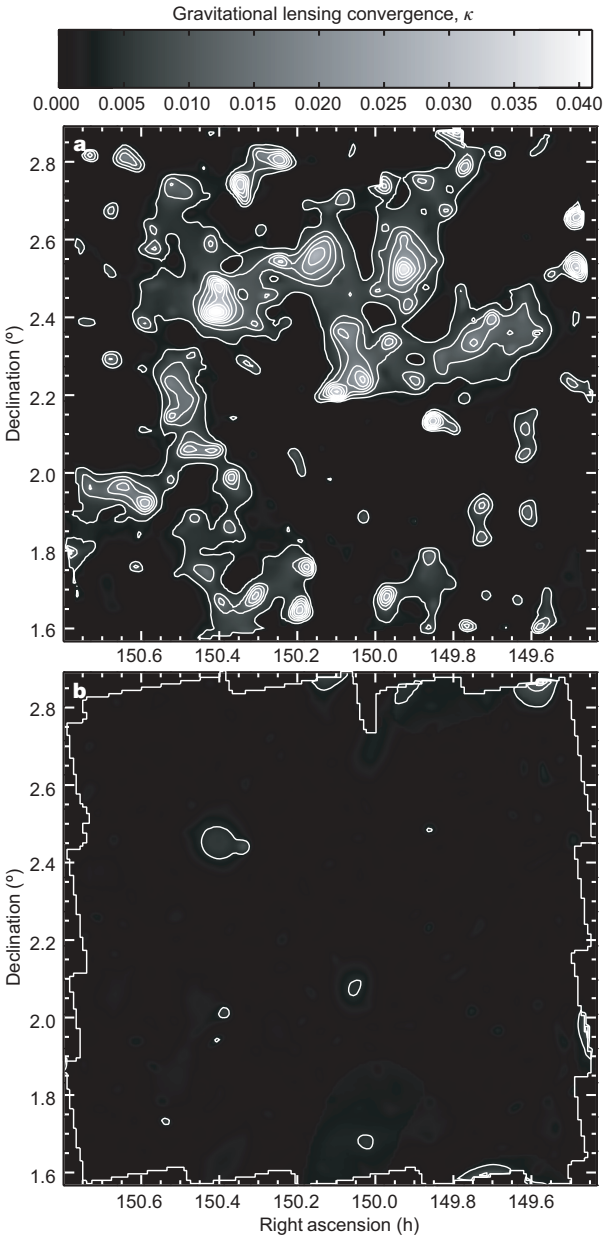

Figure 1 | Map of the dark matter distribution in the two-square-degrees COSMOS field. a, The linear greyscale shows the *E*-mode lensing convergence field κ, which is proportional to the projected mass along the line of sight. Contours begin at 0.4% and are spaced by 0.5% in κ. **b**, The absolute value of the *B*-mode signal, shown with the same greyscale and contour levels, provides a realization of the noise level in the map, plus contamination from uncorrected systematic effects; the bold outline traces the region observed with HST.

[1]California Institute of Technology MC105-24, 1200 E. California Boulevard, Pasadena, California 91125, USA. [2]Jet Propulsion Laboratory, Pasadena, California 91109, USA. [3]Laboratoire d'Astrophysique de Marseille, 13376 Marseille Cedex 12, France. [4]Max-Planck-Institut für extraterrestrische Physik, Giessenbachstraße, 85748 Garching, Germany. [5]Institute for Astronomy, Blackford Hill, Edinburgh EH9 3HJ, UK. [6]AIM, Unité Mixte de Recherche CEA, CNRS et Université de Paris VII, UMR no. 7158 CE Saclay, 91191 Gif-sur-Yvette, France. [7]Space Telescope Science Institute, 3700 San Martin Drive, Baltimore, Maryland 21218, USA. [8]Institut d'Astrophysique de Paris, Université Pierre et Marie Curie, 98 bis Boulevard Arago, 75014 Paris, France. [9]CEA/DSM/DAPNIA/SEDI, CE Saclay, 91191 Gif-sur-Yvette, France. [10]Physics Department, Ehime University, 2-5 Bunkyou, Matuyama 790-8577, Japan. [11]Department of Physics and Astronomy, University of Waterloo, Waterloo, Ontario N2L 3G1, Canada.

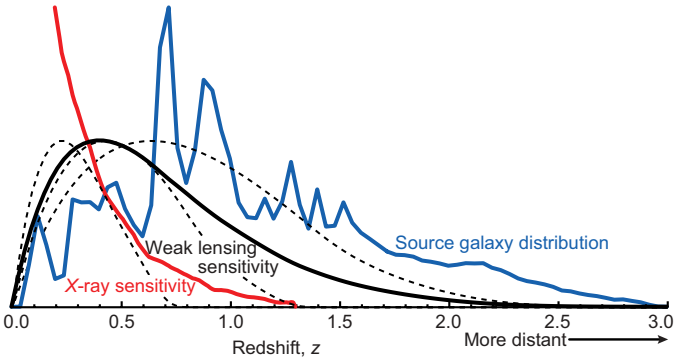

Figure 2 | Sensitivity of probes of large-scale structure, as a function of distance. The blue line shows the distribution of photometric redshifts for the source galaxies. The solid black line shows the sensitivity function of the lensing material for this source population (arbitrarily normalized to peak at unity), whereas the dashed lines show the equivalent sensitivities for the tomographic analysis. The red line shows the (arbitrarily normalized) sensitivity of the X-ray detections. Because the survey volume is a cone, the effective volumes peak at $z = 0.7$ (lensing) and $z = 0.4$ (X-rays).

contour (in both E-mode and B-mode maps) is equivalent to a $\sim 2.9\sigma$ detection threshold that includes both statistical and systematic noise.

Gravitational lensing measurements have an unusual sensitivity to the distance of the influencing mass (Fig. 2), in contrast to the familiar $\propto 1/d^2$ decline in luminosity of optically visible sources. Like an ordinary glass lens, a gravitational lens is most efficient when placed

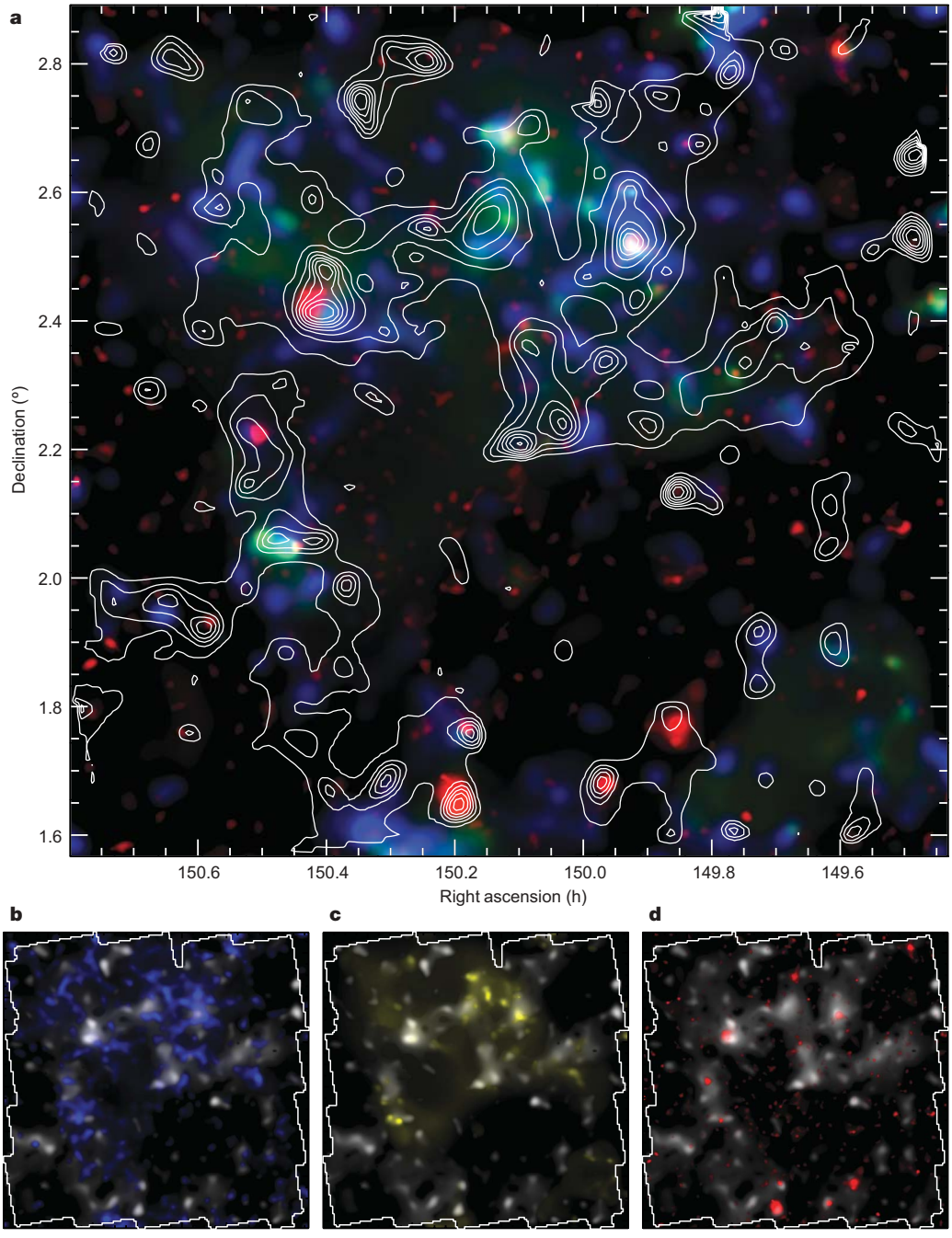

Figure 3 | Comparison of baryonic and non-baryonic large-scale structure. The total projected mass from weak lensing, dominated by dark matter, is shown as contours in **a** and as a linear greyscale in **b**, **c** and **d**. Independent baryonic tracers comprise (1) stellar mass (blue, the colour scale peaks at $2.3 \times 10^{11} M_{\rm Sun}\,{\rm deg}^{-2}$ within $\Delta z = 0.1$), (2) galaxy number density (yellow, peak at $1.4 \times 10^{5}\,{\rm deg}^{-2}$ within $\Delta z = 0.1$) seen in optical and near-infrared light (adjusted to the redshift sensitivity function of the lensing mass), and (3) hot gas (red, peak at $2.6 \times 10^{-14}\,{\rm erg\,s^{-1}\,cm^{-2}\,arcmin^{-2}}$) seen in X-rays after removal of point sources.

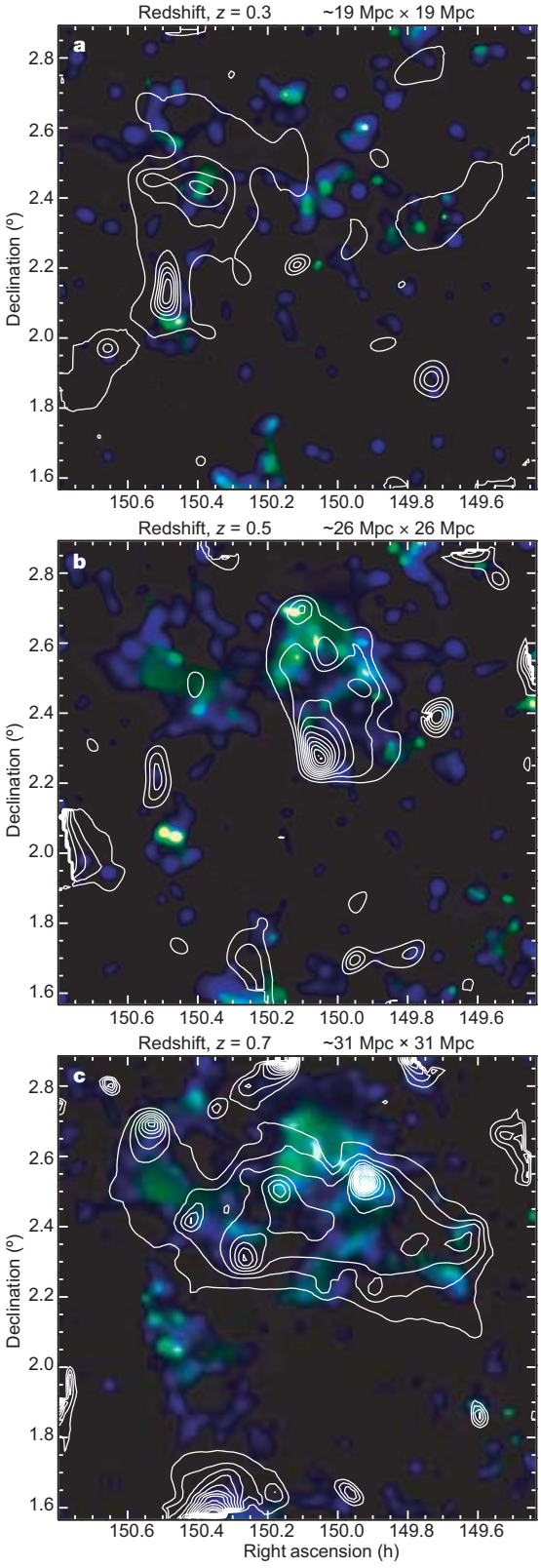

Figure 4 | Growth of large-scale structure. Slices through the evolving distribution of dark matter, created by splitting the background source galaxy population into discrete redshift slices. The sensitivity functions of the mass reconstruction peak at redshifts of ~0.3, ~0.5 and ~0.7 from **a** to **c**. Contours show the lensing convergence, in steps of 0.33%. A linear green colour ramp shows the distribution of galaxies, and blue shows their stellar mass; both are weighted with matched redshift sensitivity functions.

halfway between the source and the observer—so lensing is sensitive to neither very distant, nor very nearby structures. To compare the distribution of baryons with that of dark matter, we mimic this effect by appropriately weighting the foreground galaxies as a function of their redshift (cosmological distance). The number density of these independent galaxies, and the mass contained in their stars (estimated from their colour) provide two matched tracers of baryons. Deep X-ray observations with the XMM-Newton satellite[14] additionally highlight concentrations of hot, dense gas.

The most prominent peak in the projected, two-dimensional distributions of all four tracers (Fig. 3) is a single cluster of galaxies at (149 h 55 min, 2° 31′) and redshift $z = 0.73$. X-rays are sensitive to the square of the electron density, so they preferentially highlight the central cluster core. This cluster has an X-ray temperature $kT_X = 3.51^{+0.60}_{-0.46}$ keV and luminosity $L_X = (1.56 \pm 0.04) \times 10^{44}$ erg s^{-1} (0.1–2.4 keV band)[15]. If the cluster gas distribution were in hydrostatic equilibrium ('relaxed'), this would imply a mass of $(1.6 \pm 0.4) \times 10^{14} M_{\rm Sun}$ within an r_{500} radius of 1.4 arcminutes. However, the cluster is clearly still growing[15]. Gravitational lensing is linearly sensitive to mass, and reveals an extended dark matter halo around this cluster, which in turn lies at the nexus of several filaments. The lensing mass of the full halo is $(6 \pm 3) \times 10^{15} M_{\rm Sun}$. It is possible that such a large value includes a contribution from additional mass directly in front of the cluster, at redshifts where lensing is more sensitive. Similar projection effects might also explain the twin lensing peaks without obvious baryonic counterparts near (150 h 20 min, 2° 40′). Weak lensing analysis is very sensitive, and the map could also have been perturbed by finite-field edge effects or isolated defects in our model of the telescope's point spread function that are difficult to detect individually.

A statistical comparison across the entire map shows that baryons follow the distribution of dark matter even on large scales. The linear regression correlation coefficient r of lensing mass with stellar mass is 0.42 and r of lensing mass with galaxy number density is 0.47. The

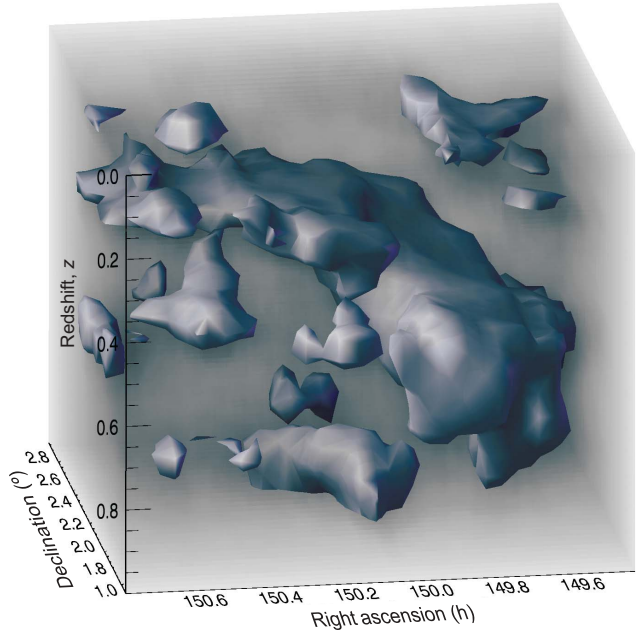

Figure 5 | Three-dimensional reconstruction of the dark matter distribution. The three axes correspond to right ascension, declination and redshift: with distance from the Earth increasing towards the bottom. The redshift scale is highly compressed, and the survey volume is really an elongated cone. An isodensity contour has been drawn at a level of $1.4 \times 10^{13} M_{\rm Sun}$ within a circle of radius 700 kpc and $\Delta z = 0.05$. This was chosen arbitrarily to highlight the filamentary structure. The faint background shows the full distribution, with the level of the greyscale corresponding to the local density. Additional views are provided in Supplementary Fig. 7.

correlation with X-ray flux is somewhat lower, 0.30, consistent with the presence of filamentary structure outside the cluster cores. The map reveals overdense regions that are topologically connected but insufficiently dense to generate X-ray emission. These filaments are not a smoothing artefact, and cannot be reproduced by adding noise to the (square root of the) X-ray image and then smoothing in a comparable way. We identify three distinct sets of environments, with a stark mass contrast. Filaments, defined as regions outside clusters but with a lensing magnification $\kappa > 0.4\%$, contain a projected number density of galaxies twice as high as that in voids, and 1.5 times lower than that in X-ray luminous clusters. Filaments have gravitationally collapsed along two axes, but clusters have continued to collapse along the third, and the galaxy number density in clusters is expected to be about five times that of filaments in the plane of the sky[16]. The observed ratio is lowered by noise in the mass reconstruction, as well as partial alignment of filaments along our line of sight.

The three-dimensional distribution of dark matter, and hence its time-dependent growth, can be visualized (Fig. 4) by splitting the background source galaxies into discrete redshift bins[17]. We have chosen bins so that the resulting foreground lensing sensitivities peak at redshifts $z \approx 0.3$, 0.5 and 0.7 (Fig. 2). These functions overlap slightly, so some structures can faintly be seen in successive slices. Catastrophic failures in photometric redshift measurement potentially mix slices further, although we have developed a method that minimizes this effect in the lensing analysis. The massive $z = 0.73$ cluster is indeed part of a much larger three-dimensional structure, including a filament partially aligned with our line of sight, which will increase its two-dimensional projected mass but not affect the X-ray flux. The corresponding *B*-mode maps (Supplementary Fig. 4) suggest that the second contours here have roughly the same 3σ significance as the first contour in Fig. 1. A full three-dimensional reconstruction of the mass distribution (Fig. 5) is obtained from the differential growth of the lensing signal between many thin slices separated by $\Delta z = 0.05$ (refs 18, 19). The evolution of this distribution is driven by the battle between gravitational collapse and the accelerating expansion of the Universe.

The independent probes of large-scale structure paint a remarkably consistent picture of the Universe on large scales. The contracting filamentary network resembles predictions from *n*-body simulations of structure formation dominated by the gravitational collapse of cold dark matter from small density perturbations in the early Universe[9]. By directly probing the distribution of mass, space-based weak lensing measurements offer the potential to link observations directly to theories that are concerned mainly with collisionless dark matter and gravity. Indeed, the resemblance of Fig. 5 to the first three-dimensional maps of the large-scale distribution of baryonic matter made by the Point Source Redshift Catalogue[20] (PSCz) fifteen years ago demonstrates substantial progress in observational astronomy.

METHODS

Shear measurement. The depth and exquisite resolution of Hubble Space Telescope images enable us to resolve the shapes of 71 galaxies per square arcminute in the F814W (approximately *I*-band) filter, with a median AB magnitude of 25.1. We use the RRG method[21] to deconvolve the galaxy shapes from the telescope's point spread function. Our processing pipeline has been calibrated on simulated HST images, and found to recover shear from galaxies in a wide range of size and flux, with less than 6% bias[12].

Mass reconstruction. The observed shear field is then converted into 'convergence' (the cumulative magnification of all lenses along a line of sight), which is proportional to the two-dimensional, projected mass[22]. The conversion is non-local, and finite-field effects introduce some defects near the edge of the map. Diversity in galaxies' intrinsic morphologies propagates into shot noise in the mass map, which we reduce by using a multiscale filtering method, based on the *à trous* wavelet transform[23], and tuned to balance completeness with minimal false detection of spurious signals[24]. Our high surface density of resolved galaxies permits a mass reconstruction with an unprecedented minimum wavelet scale (maximum resolution) of 1.2 arcminutes full-width at half-maximum (FWHM) in the projected map, and 2.4 arcminutes FWHM in the tomographic analysis. In practice, the achieved resolution of the wavelet reconstruction varies spatially with the local signal strength. Noise properties vary on the different wavelet scales, and are summed in a complex fashion that also depends upon the local signal. The noise is best quantified via the corresponding *B*-mode maps.

Charge transfer efficiency correction. One particularly troublesome systematic is introduced by image trailing during charge-coupled device (CCD) detector readout, owing to radiation damage that degrades their charge transfer efficiency (CTE)[25]. The arrangement of the ACS CCDs produces a spurious sawtooth *E*-mode convergence pattern (with an average peak signal of $\pm 0.3\%$ and a pitch of 3.3 arcminutes, corresponding to the ACS field of view); but no corresponding *B*-mode (Supplementary Fig. 2). We subtract a model[26] of the spurious signal, which incorporates parameters of galaxy flux, position on the CCD and date of exposure, from the galaxy shear catalogue. After this correction, and the removal of high-frequency information by wavelet filtering, the spurious *E*-mode convergence signal is less than 0.1% throughout the map (Supplementary Fig. 3). We note that the sharp sawtooth pattern is strongest on small scales, and systematic CTE deterioration thus limits the resolution of mass reconstruction from HST-based observations of weak lensing, at a level only just below the statistical limit set by the finite number density of resolved galaxies.

Photometric redshift measurement. Extensive follow-up observations of the COSMOS field with the Subaru, Canada–France–Hawaii (CFH), Cerro Tololo Inter-American Observatory (CTIO) 4 m and the Kitt Peak National Observatory (KPNO) 4 m telescopes[27] have provided optical and near-infrared imaging in 15 bands ranging from u^* to K_s. Such multicolour data constitutes low-resolution spectroscopy, and we use a bayesian template-fitting method[28,29] to estimate the redshift and stellar mass of each galaxy (Supplementary Fig. 5). The depth of the follow-up observations ensures completeness in stellar mass down to $7 \times 10^9\ M_{\rm Sun}$ at $z < 1.05$ (ref. 11). In the source galaxy redshift distribution (Fig. 2), the foreground peaks below $z = 1.2$ all correspond to known structures in the COSMOS field.

For galaxies fainter than those with an AB magnitude of 24.5 in the F814W filter, a characteristic degeneracy exists between galaxies at $0.1 < z < 0.3$ and $1.5 < z < 3.2$ without real spectroscopy, owing to confusion between the 4,000 Å break and coronal absorption features[27]. For the purposes of weak lensing, this degeneracy is not symmetric. Distant galaxies are viewed after significant distortion and, if placed erroneously at low redshift, would create spurious power in the nearby Universe that echoes more distant structures. On the other hand, very nearby galaxies are almost unlensed so, if placed incorrectly at high redshift, they merely dilute the signal. To deal with this redshift degeneracy, we study the joint redshift probability distribution function for each galaxy. For those with best-fitting redshifts $z < 0.4$, if any probability exists above $z > 1.5$, we move the galaxy to the weighted mean of the redshift probability integrated above $z = 1.5$. This places all uncertain galaxies in the same place, and contracts two problems into the less troublesome one. We then statistically estimate the overpopulation of high-redshift slices by comparing their apparent density of galaxies to that expected from the known galaxy luminosity function[30] (Supplementary Fig. 6).

Received 14 November; accepted 30 November 2006.
Published online 7 January 2007.

1. Zwicky, F. Die Rotverschiebung von extragalaktischen Nebeln. *Helv. Phys. Acta* **6,** 110–127 (1933).
2. Bergstrom, L. Nonbaryonic dark matter: observational evidence and detection methods. *Rep. Prog. Phys.* **63,** 793–841 (2003).
3. Clowe, D. *et al.* A direct empirical proof of the existence of dark matter. *Astrophys. J.* **648,** L109–L113 (2006).
4. Blandford, R., Saust, A., Brainerd, T. & Villumsen, J. The distortion of distant galaxies by large-scale structure. *Mon. Not. R. Astron. Soc.* **251,** 600–627 (1991).
5. Kaiser, N. Weak gravitational lensing of distant galaxies. *Mon. Not. R. Astron. Soc.* **388,** 272–286 (1992).
6. Bartelmann, M. & Schneider, P. Weak gravitational lensing. *Phys. Rep.* **340,** 291–472 (2001).
7. Refregier, A. Weak gravitational lensing by large-scale structure. *Annu. Rev. Astron. Astrophys.* **41,** 645–668 (2004).
8. Davis, M., Efstathiou, G., Frenk, C. & White, S. The evolution of large-scale structure in a universe dominated by cold dark matter. *Astrophys. J.* **292,** 371–394 (1985).
9. Springel, V. *et al.* Simulating the joint evolution of quasars, galaxies and their large-scale distribution. *Nature* **435,** 629–636 (2005).
10. Dekel, A. & Lahav, O. Stochastic nonlinear galaxy biasing. *Astrophys. J.* **520,** 24–34 (1999).
11. Scoville, N. *et al.* COSMOS: Hubble Space Telescope observations. *Astrophys. J.* (in the press).
12. Leauthaud, A. *et al.* COSMOS: ACS galaxy catalog. *Astrophys. J.* (submitted).
13. Schneider, P., van Waerbeke, L. & Mellier, Y. B-modes in cosmic shear from source redshift clustering. *Astron. Astrophys.* **389,** 729–741 (2002).

14. Hasinger, G, *et al.* The XMM-Newton wide-field survey in the COSMOS field: I. Survey description. *Astrophys. J.* (in the press).
15. Guzzo, G. *et al.* A large-scale stucture at $z=0.73$ and the relation of galaxy morphologies to local environment. *Astrophys. J.* (submitted).
16. Shen, J., Abel, T., Mo, H. & Sheth, R. An excursion set model of the cosmic web: the abundance of sheets, filaments, and halos. *Astrophys. J.* **645,** 783–791 (2006).
17. Massey, R. *et al.* Weak lensing from space: II. Dark matter mapping. *Astron. J.* **127,** 3089–3101 (2004).
18. Bacon, D. & Taylor, A. Mapping the 3D dark matter potential with weak shear. *Mon. Not. R. Astron. Soc.* **344,** 1307–1326 (2003).
19. Taylor, A. *et al.* Mapping the 3D dark matter with weak lensing in COMBO-17. *Mon. Not. R. Astron. Soc.* **353,** 1176–1196 (2003).
20. Saunders, W. *et al.* Density and velocity fields from the PSCz survey. In *Towards an Understanding of Cosmic Flows* (eds Courteau S., Strauss M. & Willick, J) *ASP Conf. Ser.*, **201,** 228–236 (Astronomical Society of the Pacific, San Francisco, 1999).
21. Rhodes, J., Refregier, A. & Groth, E. Weak lensing measurements: a revisited method and application to Hubble Space Telescope images. *Astrophys. J.* **536,** 79–100 (2000).
22. Kaiser, N. & Squires, G. Mapping the dark matter with weak gravitational lensing. *Astrophys. J.* **404,** 441–450 (1993).
23. Starck, J.-L. & Murtagh, F. *Astronomical Image and Data Analysis* 2nd edition (Springer, Heidelberg, 2006).
24. Starck, J.-L., Pires, S. & Refregier, A. Weak lensing mass reconstruction using wavelets. *Astron. Astrophys.* **451,** 1139–1150 (2006).
25. Hopkinson, G., Dale, C. & Marshall, P. Proton effects in charge-coupled devices. *IEEE Trans. Nucl. Sci.* **43,** 614–627 (1996).
26. Rhodes, J. *et al.* Removing the effects of the Advanced Camera for Surveys point spread function. *Astrophys. J.* (submitted).
27. Capak, P. *et al.* Photometric redshifts of galaxies in COSMOS. *Astrophys. J.* (submitted).
28. Benítez, N. Bayesian photometric redshift estimation. *Astrophys. J.* **536,** 571–583 (2000).
29. Mobasher, B. *et al.* The first release COSMOS optical and near-IR data and catalog. *Astrophys. J.* (submitted).
30. Steidel, C. *et al.* A study of star-forming galaxies in the $1.4<z<2.5$ redshift desert: overview. *Astrophys. J.* **604,** 534–550 (2004).

Supplementary Information is linked to the online version of the paper at www.nature.com/nature.

Acknowledgements This work was based on observations with the NASA/ESA Hubble Space Telescope, obtained at the Space Telescope Science Institute, which is operated by the Association of Universities for Research in Astronomy, Inc. (AURA). We also used data collected from: the XMM-Newton, an ESA science mission with instruments and contributions directly funded by ESA member states and NASA; the Subaru Telescope, which is operated by the National Astronomical Observatory of Japan; the European Southern Observatory, Chile; the Kitt Peak National Observatory, the Cerro Tololo Inter-American Observatory, and the National Optical Astronomy Observatory, which are operated by AURA under cooperative agreement with the American National Science Foundation; the National Radio Astronomy Observatory, which is a facility of the American National Science Foundation operated under cooperative agreement by Associated Universities, Inc.; and the Canada-France-Hawaii Telescope operated by the National Research Council of Canada, the Centre National de la Recherche Scientifique de France and the University of Hawaii. The photometric redshifts used here were validated using spectra from the European Southern Observatory Very Large Telescope zCOSMOS survey. We gratefully acknowledge the contributions of the entire COSMOS collaboration, consisting of more than 70 scientists. We thank T. Roman, D. Taylor and D. Soderblom for help scheduling the extensive COSMOS observations; and A. Laity, A. Alexov, B. Berriman and J. Good for managing online archives and servers for the COSMOS data sets at NASA IPAC/IRSA. This work was supported by grants from NASA (to N.S. and R.M.).

Author Contributions A.K. processed the raw HST data, and J.-P.K. masked defects in the image. A.L., J.R. and R.M. catalogued the positions and shapes of galaxies. Y.T. and S.S. obtained multicolour follow-up data, which was processed and calibrated by S.S., P.C., H.McC. and H.A. P.C. determined galaxies' redshifts, and B.M. their stellar mass. N.S. constructed maps of stellar mass and galaxy density. A.F. processed the X-ray image and removed point sources. R.M. and A.R. produced the two-dimensional and tomographic mass maps; J.-L.S. and S.P. developed the wavelet filtering technique. D.B. and A.T. produced the three-dimensional mass reconstruction. J.T., A.F., R.E. and R.M. compared the various tracers of large-scale structure.

Author Information Reprints and permissions information is available at www.nature.com/reprints. The authors declare no competing financial interests. Correspondence and requests for materials should be addressed to R.M. (rjm@astro.caltech.edu).